Diamond & Related Materials 52 (2015) 1–10

Contents lists available at ScienceDirect

Diamond & Related Materials

journal homepage: www.elsevier.com/locate/diamond

Probing optical, phonon, thermal and defect properties of 3C–SiC/Si (001)

Devki N. Talwar

Department of Physics, Indiana University of Pennsylvania, 975 Oakland Avenue, 56 Weyandt Hall, Indiana, PA 15705-1087, USA

ARTICLE INFO

Article history:
Received 1 July 2014
Received in revised form 8 November 2014
Accepted 24 November 2014
Available online 28 November 2014

Keywords:
3C-SiC/Si (001)
Optical, phonon and defect properties
Raman scattering spectroscopy
Green's function theory
Gap-modes of anti-site pair defect

ABSTRACT

Comprehensive results of experimental and theoretical studies are reported to probe the optical, phonon, thermal and defect properties of 3C–SiC/Si (001). By exploiting phonon-assisted Raman scattering (RS) spectroscopy we have recognized, among the conventional optical modes [TO(Γ) ~796 cm^{-1} and LO(Γ) ~973 cm^{-1}], two extra phonon features near ~625 cm^{-1} and 670 cm^{-1} — possibly falling between the forbidden gap of the acoustic and optical branches. Temperature dependent profile of the unresolved ~670 cm^{-1} band has indicated disordering by nearby defects and/or stress — rendering shorter phonon lifetime to instigate mode broadening. Accurate assessments of the lattice dynamical, thermal and defect properties are achieved by exploiting phonons from a rigid-ion model fitted to the inelastic x-ray scattering data and expending apposite group-theoretical selection rules. Lattice relaxations around Si/C atoms attained by the first-principles bond-orbital model for isolated defects have helped us to evaluate the necessary force constant variations for constructing perturbation matrices of the "complex-defect-centers". For isolated anti-site C_{Si} and Si_C defects (T_d-symmetry), our methodical Green's function (GF) theory has predicted triply degenerate F_2 gap modes near 630 cm^{-1} and 660 cm^{-1}, respectively. The GF simulations of impurity vibrations for a neutral nearest-neighbor anti-site Si_C–C_{Si} pair-defect (C_{3v}-symmetry) provided gap-modes to appear within the broad ~670 cm^{-1} band at 664.8 cm^{-1} (a_1) and 660.6 cm^{-1} (e). The calculated results of localized vibrational modes are compared and discussed with phonon features observed in the RS experiments as well as with the density function theory.

1. Introduction

The exceptional electrical, mechanical, thermal and chemical properties have made silicon carbide (SiC) one of the most suitable semiconductors for fabricating high-power and high-temperature electronics, micro-electro-mechanical systems (MEMS), optoelectronic devices and sensors [1–5]. The suitability of SiC in engineering microelectronic devices for high radiation flux environments, high-power and high-temperature applications is largely related to its wide bandgap [6–11] and large Si–C bond strength. In SiC networks, the bonds between Si–C atoms are characterized by an sp^3 bonding to form close-packed tetrahedral unit cells. Depending upon the stacking sequence of the Si–C units, there exists a large number (>200) of crystallographic forms or polytypes. The most common ones are 2H, 4H, 6H and 3C–SiC — where the letters in the labels represent the types of crystal structures (i.e., H for hexagonal and C for cubic or zinc-blende (*zb*)) and the number refers to Si–C bi-layers per unit cell. While thin epitaxial films of 6H–(4H)–SiC are grown at higher temperature (>1450 °C) on commercially available substrates – the growth of *zb* or cubic 3C–SiC films on Si that requires lower (~1350 °C) temperature – i.e., below the Si melting temperature, has been a challenge [12–16]. The improvement in crystal quality since its inception in the late 1980's, and the potential of lower production cost and easier integration with Si technology, have rekindled new interest in 3C–SiC as an attractive alternative to 4H– and 6H–SiC.

Due to significant differences in both the lattice constants (19.8%) and coefficients of thermal expansion (CTE) (8%) between 3C–SiC and Si, a large number of crystalline defects are formed at the 3C–SiC/Si interface. For the heteroepitaxial growth of 3C–SiC on Si (001) substrates, several processes reported in the literature have employed either the horizontal [12–16] (H) or vertical [17] (V) chemical vapor deposition (CVD) reactors. The question of assessing local arrangement of constituent atoms is, however, still a matter of debate. Especially, an understanding of the atomic structures of various "intrinsic-defects" is imperative for the improvements of SiC's electrical, optical and device characteristics. This is notably true for the low temperature (LT) photoluminescence (PL) D_I center, known for decades [18]. While the D_I center has exhibited two closely spaced gap-modes [19–25] (661.3 cm^{-1} and 668.7 cm^{-1}) in 3C–SiC — its atomic structure impacting the vibrational features has not yet been completely understood. Given these issues there is a compelling reason for further investigations of the structural, phonon, thermodynamic and defect characteristics of 3C–SiC.

Raman scattering (RS) spectroscopy is a very useful, sensitive and non-destructive technique used for establishing crucial optical, phonon and defect parameters in semiconductors [26]. The synchrotron radiation extended x-ray absorption fine structure (SR-EXAFS) also provides indispensable structural information about the materials by careful analysis of

E-mail address: talwar@iup.edu.

http://dx.doi.org/10.1016/j.diamond.2014.11.011
0925-9635/

their x-ray absorption spectra [27]. Quite recently, we have performed comprehensive RS, PL and SR-EXAFS measurements and extracted valuable lattice dynamical parameters related to the structural quality of V-CVD grown 3C–SiC/Si (001) material samples [28]. In the first-order RS, besides observing the conventional long-wavelength $\vec{q} \sim 0$ optical modes of 3C–SiC [TO(Γ) ~794 cm^{-1}, LO(Γ) ~973 cm^{-1}] we have recognized two additional phonon bands near ~625 cm^{-1} and 670 cm^{-1}. It is likely that these extra defect modes may fall between the forbidden gap of the acoustic and optical branches of 3C–SiC. Again, the emergence of a relatively broad unresolved Raman band near ~670 cm^{-1} [28] lies close to a doublet (661.3 cm^{-1} and 668.7 cm^{-1}) ascribed earlier to the D_I optical center and correlated to close-by "Si_C–C_{Si}" anti-site pair (ASP) defects in 3C–SiC. In semiconductors, it is often quite difficult to establish a unique relationship between experimental results (especially from the PL excitation, RS and/or Zeeman studies) to a specific type of defect center. One, therefore, very much requires applying credible theoretical methods to simulate experimental data on the dynamical and/or electronic behavior of complex defects to help identify the plausible atomic structures of diverse optical centers.

The purpose of this paper is to report the results of a comprehensive experimental and theoretical study (cf. Section 2) to probe the optical, lattice dynamical, thermal and defect properties of 3C–SiC/Si (001). The 'Si–C' and 'Si–Si' bond lengths are appraised by a careful analysis of the recent SR-EXAFS data [28]. Accurate assessments of the lattice dynamical, thermal and defect properties are attained by exploiting phonons from a realistic rigid-ion model (RIM) [29] fitted to the inelastic x-ray scattering (IXS) [30] data (cf. Sections 2.1–2.9) and expending the pertinent group-theoretic selection rules. The relaxation around Si/C atoms accomplished for isolated defects by first-principles bond-orbital model (BOM) has assisted us in evaluating the necessary force constant variations [31,32] to simulate the localized vibrational modes (LVMs) of various defect-centers (cf. Section 2.4–2.9) using Green's function (GF) methodology [33]. The lattice dynamical calculations are reported for both perfect and imperfect 3C–SiC and the results are compared with the existing experimental/theoretical [34–41] data. The outcome of this study is discussed in Section 3 with a summary of concluding remarks presented in Section 4.

2. Theoretical details

For empathizing the phonon properties of perfect semiconductors [42–45] and to understand the dynamical behavior of imperfect materials by GF technique, an accurate knowledge of the host lattice phonons is a prerequisite [29]. As compared to the *ab initio* calculations [20–25], the advantage of employing the GF theory is that it yields correct spectral functions and impurity traits to correlate them with optical experiments. To comprehend thermo-dynamical properties, assessing critical-point phonon energies from second-order Raman scattering (SORS) spectroscopy and evaluating the impurity vibrational modes in 3C–SiC we have incorporated the host lattice phonons from a RIM [29] fitted to the IXS [30] data.

2.1. Lattice dynamics

To compute the lattice dynamics of perfect 3C–SiC using RIM, we have assumed that the polarization of the *zb* crystal is completely determined by the displacements of point ions from their equilibrium positions i.e., the ions are considered to be rigid and non-polarizable. In this scheme, the atomic displacements of j^{th} vibrational mode can be written in terms of the plane waves of wave-vector $\vec{q}$ and frequency $\omega_j(\vec{q})$ [29]:

$$u_\alpha\left(l\kappa|\vec{q}\,j\right) = \frac{1}{\sqrt{M_\kappa}} e_\alpha\left(\kappa|\vec{q}\,j\right) e^{i\left[\vec{q}\,.\,\vec{x}(l\kappa)-\omega_j\left(\vec{q}\right)t\right]}, \tag{1}$$

where t is the time; $\vec{x}(l\kappa)$ and M_κ are, respectively the position and the mass of the $(l\kappa)$ atom.

In the harmonic approximation, the equations of motion for *zb* materials within the rigid-ion model approach take the form:

$$\omega_j^2\left(\vec{q}\right) e_\alpha\left(\kappa\left|\vec{q}\,j\right.\right) = \sum_{\kappa'\beta} D^{sC}_{\alpha\beta}\left(\kappa\kappa'\left|\vec{q}\right.\right) e_\beta\left(\kappa'|\vec{q}\,j\right) \;;\; \kappa,\kappa' = 1,2 \quad , \tag{2}$$

where, $D^{sC}_{\alpha\beta}\left(\kappa\kappa'\left|\vec{q}\right.\right)$ is the dynamical matrix comprised of both the short-range $D^{s}_{\alpha\beta}\left(\kappa\kappa'\left|\vec{q}\right.\right)$, and long-range Coulomb $D^{C}_{\alpha\beta}\left(\kappa\kappa'\left|\vec{q}\right.\right)$ components [29]. For 3C–SiC, we have assessed all the short-range forces (A, B, C_κ, D_κ, E_κ and F_κ) up to second-nearest neighbors and long-range (Ze) Coulomb interactions following successive least-square fitting procedures [33] by incorporating the critical point phonon energies, lattice constant, as well as elastic constants [34–45].

The best fit results of phonon dispersions between IXS [30] and RIM [29] calculations are reported in Fig. 1a). A comparison of the critical point phonon energies (see: Table 1) has provided a very good agreement with the existing experimental and theoretical data. By incorporating phonons at the mesh of 64,000 $\vec{q}$ points in the Brillouin zone (BZ) and following standard practices, we have computed one–phonon g (ω), (see: Fig. 1b)) and two–phonon $g_\pm$ (ω), (see: Fig. 1c)) density of states (DOS) for 3C–SiC. The phonon sampling widths used in the calculations of $g(\omega)$ and $g_\pm(\omega)$ are set at $\Delta\omega = \omega_{LO(\Gamma)}$ / 100 and $\omega_{LO(\Gamma)}$/ 50, respectively. Due to a large mass difference between Si (28.09 amu) and C (12.01 amu) atoms, a wider (see: Fig. 1b)) phonon gap (622–740 cm^{-1}) is identified between the acoustic and optical phonon branches. For 3C–SiC, the simulated results of lattice dynamics are proven imperative for establishing the specific phonon features (i.e., gap modes) of various intrinsic defects (cf. Sections 2.4–2.9) perceived in several optical experiments [20–25].

2.2. Thermodynamic properties

As compared to many refractory materials, the specific heat of SiC polytypes is established to have higher value with dominant contributions to $C_v(T)$ emanating from their lattice phonons. To acquire the specific heat in solids [35–41], it is necessary to evaluate the total internal energy due to thermal vibrations of atoms. By assuming a Planck's-distribution of harmonic oscillators, the internal energy Φ_{vib} of lattice phonons having frequencies $\omega_j\left(\vec{q}\right)$ can be expressed as:

$$\Phi_{vib} = \frac{1}{2}\sum_{j,\vec{q}} \hbar\omega_j\left(\vec{q}\right) + k_B T \sum_{j,\vec{q}} \ln\left[1 - e^{-\frac{\hbar\omega_j\left(\vec{q}\right)}{k_B T}}\right] \quad , \tag{3}$$

where, k_B is the Boltzmann constant.

In quasi-harmonic approximation, the heat capacity $C_v(T)$ can be obtained by differentiating Eq. (3) with respect to the temperature, i.e.

$$C_v(T) = \sum_{j,\vec{q}} k_B \left(\frac{\hbar\omega_j\left(\vec{q}\right)}{k_B T}\right)^2 \left(\frac{e^{\frac{\hbar\omega_j\left(\vec{q}\right)}{k_B T}}}{\left[e^{\frac{\hbar\omega_j\left(\vec{q}\right)}{k_B T}} - 1\right]^2}\right). \tag{4}$$

From the Debye equation for the specific-heat C_v(T)

$$C_v(T) = 9k_B r\left(\frac{T}{\Theta_D(T)}\right)^3 \int^{\Theta_D(T)/T} \frac{x^4 e^x}{(e^x - 1)^2} dx \quad , \tag{5}$$

one can easily obtain Θ_D(T).

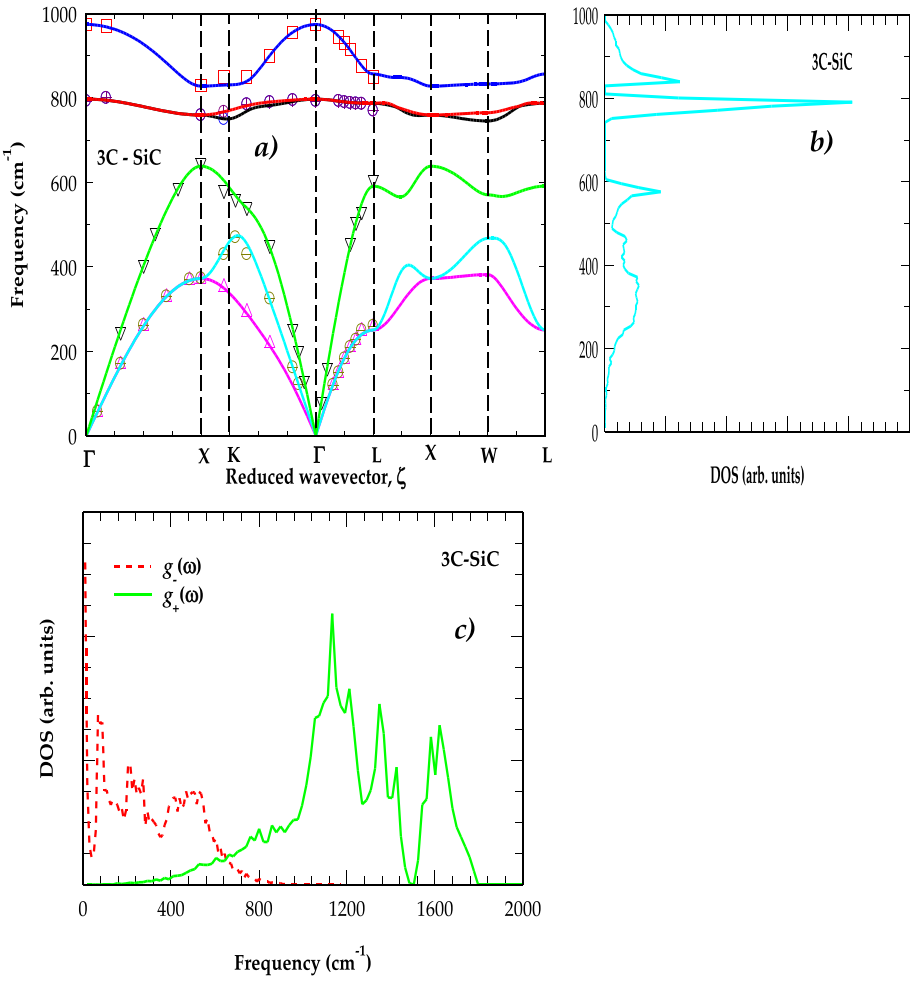

Fig. 1. (a) Experimental (△, □, ▽, ⊕, ▽) [30] and calculated solid lines (–) phonon dispersion curves along high-symmetry directions based on rigid-ion model [29] along high-symmetry directions (b) one-phonon density of states g(ω) and (c) two-phonon density of states $g_{\pm}(\omega)$ for 3C–SiC (see text).

By incorporating phonons of 3C–SiC (cf. Section 2.1) from a RIM [29], the calculated results of temperature dependent Θ_D(T) (see: Fig. 2a)) and C_v(T) (see: Fig. 2b)) are displayed along with the existing experimental and theoretical data [37–41]. Except for the higher temperatures (>700 K) a very good agreement is achieved between the simulated and experimental $\Theta_D(T)$ values [40]. In Table 1, the results listed for $\Theta_D(T)$ and C_v(T) at T → 0 and 300 K are compared with the available results from the literature [37–41]. Again, at higher T our RIM calculation of C_v(T) approaches 3R value (see Fig. 2b)) — in excellent agreement with the Dulong and Petit [46] rule. At T < Θ_D, one would expect to have contributions to C_v(T) in solids from both electrons (very small) and phonons. In 3C–SiC, however, our study has offered an insignificant effect of the electrical heat conduction to C_v(T) up to ~1000 K — as the covalently bonded material is essentially an electrical insulator.

2.3. Second-order Raman scattering in perfect crystals

Many microscopic theories have been exploited for comprehending SORS processes [42–45] in solids. In such schemes, the complexities involved in the higher-order scattering terms have made numerical simulations of the RS intensity profiles rather strenuous. On the other hand, phenomenological theories of SORS are discerned to be equally useful for gaining qualitative insights of the phonon processes involved in RS experiments. In RS, the intensity of light scattered by lattice vibrations of a crystal per unit time into a solid angle $d\Omega$ is given by [42]:

$$I(\omega_s)d\Omega = \frac{\hbar\omega_i^4}{2\pi^2c^3}\sum_{r=1}^{2}\sum_{\substack{\alpha\beta\\ \gamma\delta}} n_\alpha^r n_\beta^r i_{\alpha\beta\gamma\delta}(\omega)E_\gamma^- E_\delta^+ d\Omega \quad ;a,\beta,\delta = x,y,z \quad , \quad (6)$$

where, the term ω ($\equiv\omega_i - \omega_s$) with ω_i and ω_s represent the frequencies of incident and scattered photons, respectively; c is the speed of light; $\vec{n}_\alpha^1$ and $\vec{n}_\beta^2$ are mutually perpendicular unit vectors —also perpendicular to the direction of propagation of the scattered light; E_γ^- and E_δ^+ are the components of the incident electric field.

At zero temperature, the term $i_{\alpha\beta\gamma\delta}(\omega)$ for the SORS in solids can be expressed as [47]:

$$i_{\alpha\beta\gamma\delta}(\omega) = \frac{1}{2}\sum_{\vec{q}\,jj'} P_{\alpha\beta}\left(\vec{q}|jj'\right)P_{\gamma\delta}\left(\vec{q}|jj'\right) \times \delta\left(\omega - \left|\omega_j\left(\vec{q}\right) \pm \omega_{j'}\left(\vec{q}\right)\right|\right) \quad , \quad (7)$$

where $P_{\alpha\beta}\left(\vec{q}|jj'\right)$ is a second-order polarizability-tensor representing change in $\alpha\beta$ component of the crystal polarizability due to the presence of two-lattice phonons. Clearly, the predicament of modelling the SORS using Eq. (7) reduces to: (i) the calculation of phonons [i.e., $\omega_j\left(\vec{q}\right)$ and

Table 1
Comparison of the calculated phonon frequencies (in wave numbers) at high symmetry critical points in the BZ, Debye temperatures Θ_D (in °K) and specific heat C_v (in J/mole °K) with the experimental and theoretical data for 3C–SiC.

Point group	Modes	IXS[a]	Exptl.[b]	Our	Theory[a]	Theory[c]	Theory[d]
T_d	LO(Γ)	–	972	974	974.8	945	956
	TO(Γ)	793	796	797	793.1	774	783
D_{2d}	LO(X)	–	830	828	834.4	807	829
	TO(X)	759	763	760	763.8	741	755
	LA(X)	644	640	639	635.1	622	629
	TA(X)	373	373	373	370.2	361	366
C_{3v}	LO(L)	–	838	857	845.6	817	838
	TO(L)	758	766	787	767.1	747	766
	LA(L)	615	610	591	615.9	601	610
	TA(L)	265	266	251	263.6	257	266
C_s	O_1(K)	849		832			
	O_2(K)	–		771			
	O_3(K)	758		751			
	A_1(K)	565		587			
	A_2(K)	450		461			
	A_3(K)	368		337			
S_4	O_1(W)			837			
	O_2(W)			779			
	O_3(W)			777			
	A_1(W)			576			
	A_2(W)			393			
	A_3(W)			301			
	Θ_D(min)	–		899			
	$\Theta_D(T \to 0)$	1080[e]		1080			
	$\Theta_D(T \to 800)$	1270[f]		1186			
	$C_v(T \to 298)$	26.84[f]		26.24			

[a] Ref.[30].
[b] Ref. [34].
[c] Ref. [35].
[d] Ref. [36].
[e] Ref. [40].
[f] Ref. [41].

$e_\alpha\left(\kappa\middle|\vec{q}\,j\right)$], (*ii*) determining the phonon-dependent polarizability coefficients $P_{\alpha\beta}\left(\vec{q}\middle|jj'\right)$ and (*iii*) evaluating the two-phonon DOS. Following Karo et al. [47] and assuming the polarizability tensors as constants we have exploited the RIM phonons to simulate DOS [$g_\pm(\omega)$] for 3C–SiC.

It is true that the SORS can emanate from any $\vec{q}$-point in the BZ [42–45] — the spectra become stronger, however, at larger phonon wave-vectors [i.e., X (1,0,0), L (1/2,1/2,1/2) and W (1,1/2,0)] near the BZ boundary. Consequently, the scattering mechanisms at critical points X, L and W are responsible [48–50] for the observed sharp RS features [28] (see: Fig. 3a–b)) and can be associated with peaks in the simulated $g_\pm(\omega)$. At the center of the BZ, while the Γ critical-point initiates flattening of the phonon dispersion — it does not stimulate, however, the high DOS. In Fig. 3b) we have compared the polarization dependent RS results for a 16 μm free standing film [28] with the simulated $g_+(\omega)$. It is to be noted that the two stronger SORS phonon features near 1520 cm^{-1} and 1714 cm^{-1} are assigned to 2TO (X) and 2TO (L), respectively.

By appraising the SORS (see: Fig. 3a–b)) [28] with the calculated $g_\pm(\omega)$ (see: Fig. 2c)), we have divided the experimental spectra into three regimes: *a*) a low frequency region below < ~794 cm^{-1} — controlled by the transverse acoustic (overtones/combinations) and opical–acoustic and/or acoustic phonon differences (i.e., LO–LA; TO–TA; LA–TA), *b*) a moderate frequency regime with modes falling between ~975–1475 cm^{-1} – dominated by the optical–acoustic phonons

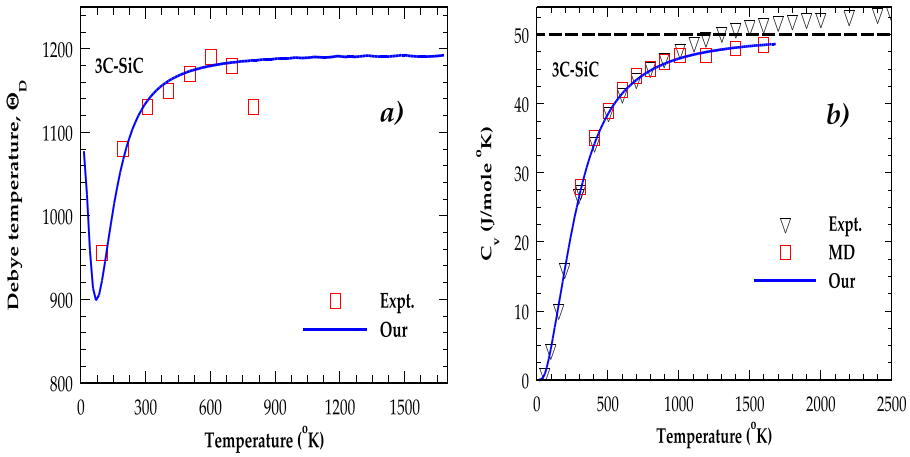

Fig. 2. (a) Calculated Debye temperature Θ_D as a function of *T* (–) based on rigid-ion model [29], compared with experimental data (□) [40]. (b) Calculated specific heat C_V (T) as a function of *T* (–) based on rigid-ion model [29], compared with experimental and theoretical data (□,▽) [37,41].

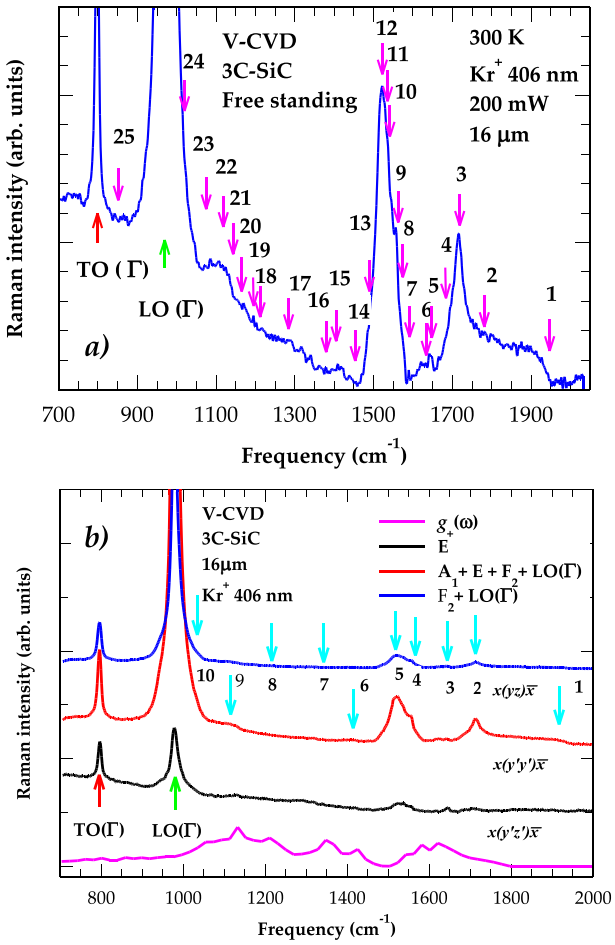

Fig. 3. (a) Room temperature second-order Raman spectrum (SORS) from a 16 μm free standing V-CVD grown 3C–SiC film [28] activating two-phonon modes (overtones and combinations) represented by 1–25 arrows (magenta color); (b) experimental results of polarization dependent SORS in the notations of with major RS peaks (1–10) represented by blue colored arrows compare favorably well with the simulated two-phonon DOS $g_+(\omega)$.

(overtones/combinations), and *c*) a high frequency region above >1475 cm^{-1} – governed by the optical phonons (overtones/combinations) [48–50]. Although the major features observed in the polarization dependent SORS (see: Fig. 3b)) for a 16 μm free standing film [28] compare favorably well with $g_+(\omega)$ — a more quantitative interpretation of the spectra (Fig. 3a)) is made (see: Table 2) using RIM phonons fitted to the IXS data and by expending apposite group-theoretic selection rules [47–50].

2.4. Raman scattering of imperfect 3C–SiC

Similar to the perfect crystals (cf. Section 2.3), it is equally possible to expand relationships (Eq. 6) between the intensity of incident and scattered electromagnetic fields to evaluate RS profiles in imperfect solids [51]. We expect that a careful analysis of the vibrational fingerprints by RS will also help extort valuable information about the nature of defects present in V-CVD grown 3C–SiC/Si (001) samples. In the first-order RS, the wave vector and polarization selection rules near $\vec{q} \approx 0$ hold strictly for the perfect crystals. In the imperfect solids, the presence of defects causes the loss of periodicity and reduction in crystal symmetry. One, therefore, anticipates breakdown of the polarization selection rules that could initiate impurity vibrational bands to appear at the forbidden configurations while the reduced phonon lifetime to instigate mode broadening. For the *zb* type materials, a complete description of the GF methodology to simulate impurity-induced first-order RS is reported in Ref. [33] and will not be repeated here. However, we have summarized (cf. Sections 2.5–2.7) the pertinent portion of the GF theory [33] required to elucidate lattice dynamics of both isolated (T_d-symmetry) and complex-defect centers including ASP "Si_C–C_{Si}" defects (C_{3v}-symmetry) that best explained the gap modes and phonon broadening of an unresolved ~670 cm^{-1} mode observed in RS experiments [28].

2.5. GF theory of isolated defects

Before presenting a succinct GF theory for understanding the vibrational modes of nearest-neighbor (NN) pair-defects, we have focused first on the dynamical behavior of a single isolated defect having T_d-symmetry (see: Fig. 4a)) where an impurity atom occupies either the Si-site ($\kappa = 1$) or the C-site ($\kappa = 2$) in 3C–SiC. In the framework of a RIM, the perturbation matrix $\boldsymbol{P}$ includes changes in atomic mass at the impurity site denoted by ε_1 [$\equiv(M_1 - M_1^l)/M_1$] or ε_2 [$\equiv(M_2 - M_2^l)/M_2$], and the force constant variations indicated by t (1–2, 1–3, 1–4, 1–5) or u (2–1, 2–6, 2–7, 2–8) between the impurity and its relevant NN bonds. The erection of full-size 15 × 15 $\boldsymbol{G_o}$ and $\boldsymbol{P}$ matrices has been reported in Ref. [33]. By taking into account of the point group symmetry, we have simplified $\boldsymbol{G_o}$ and $\boldsymbol{P}$ matrices into smaller size blocks corresponding to the irreducible representations of T_d symmetry

$$\Gamma_{T_d} = A_1 \otimes E \otimes F_1 \otimes 3F_2. \tag{8}$$

For single isolated defects, while the three A_1, E and F_2 types of vibrational modes are Raman active the triply degenerate F_2 mode is only IR active.

2.6. GF theory of pair defects

The NN pair-defect involves two impurity atoms (see: Fig. 4b)) occupying lattice sites 1 and 2, respectively — causing changes in the masses (ε_1, ε_2) at impurity sites and variations in the force constants (t, u) between 'impurity-host' atoms. An effective force constant F_{12} ($\equiv u + t - ut + \Gamma_{12}$) is included here (see: Ref. [33] using Γ_{12}) to account for the changes in u and t of isolated impurities involved in the formation of a pair-defect. The term $F_{12} < 0$ (or > 0) signifies stiffening (or softening) between the impurity pair-bond. Again, the point group symmetry of a NN 'pair-defect' is C_{3v} with axis along the pair-bond involving eight atoms — causing the size of defect space to increase to 24 × 24. The total representation of $\Gamma_{C_{3v}}$ in the 24-dimensional space, reported by Ludwig and Woodbury [52] is used here to block-diagonalize $\boldsymbol{G_o}$ and $\boldsymbol{P}$ matrices with each block along the diagonal belonging to the following irreducible representations:

$$\Gamma_{C_{3v}} = 6a_1 \otimes 2a_2 \otimes 8e \ . \tag{9}$$

Again, from the Group-theoretical analysis [52], it has been perceived that since impurity atoms in the pair-defect remain stationary in the a_2 representation — only a_1 and e types of modes are optically (IR and Raman) active. As the degeneracies are lifted at the defect sites, one expects observing four LVMs for the pair-defect having very light impurity atoms: *two* non-degenerate modes due to the movement of impurity atoms along the pair-bond [i.e., ω_1 ($a_1^+ \leftarrow\rightarrow$) and ω_4 ($a_1^- \rightarrow\rightarrow$)] and *two* doubly-degenerate modes as a result of their vibration perpendicular to it [i.e., ω_2 ($e^+ \uparrow\downarrow$) and ω_3 ($e^- \uparrow\uparrow$)] generally with $\omega_1 > \omega_2 > \omega_3 > \omega_4$. However, the number of vibrational modes can differ if one of the impurity masses in the pair-defect is heavier than the host lattice atom and/or having strongly modified interactions.

By deliberating the appropriate perturbation matrices of both isolated and/or pair defects one can obtain the frequencies of their local and/or

Table 2
Second-order Raman spectrum of a V-CVD grown 3C–SiC 16 μm thick free standing film. The observed peak positions marked by numbers 1–25 with characteristic frequency (cm^{-1}) are assigned on the basis of RIM phonons using Group-theoretic selection rules [48,49].

Number of peaks		Assignment[a]	Calculated	Experimental	Symmetry
Fig. 3a	Fig. 3b		frequency (cm^{-1})	frequency (cm^{-1})	
1	1	2LO(Γ)	1948	1946	A_1
2	2	LO(Γ)+TO(Γ)	1771	1775	$A_1(F_2)$
3		2LO(L)	1714	1712	$A_1(F_2)$
4	3	$2O_1$(W)	1674	1678	A_1, F_2
5		2LO(X)	1656	1652	$A_1(F_2)$
6		LO(L)+TO(L)	1644	1640	A_1, F_2
7		2TO(Γ)	1594	1592	$A_1(F_2)$
8		LO(X)+TO(X)	1588	1585	A_1, F_2
9	4	2TO(L)	1574	1575	$A_1(F_2)$
10		$2O_2$(W)	1558	1560	A_1, F_2
11		$2O_3$(W)	1554	1556	A_1, F_2
12	5	2TO(X)	1520	1522	$A_1(F_2)$
13		LO(X)+LA(X)	1467	1470	A_1, F_2
14		LO(L)+LA(L)	1448	1450	A_1, F_2
15	6	TO (X)+ LA (X)	1399	1402	$A_1(F_2)$
16	7	TO(L)+LA(L)	1378	1376	A_1, F_2
17	8	2LA(X)	1278	1280	A_1, F_2
18		LO(X)+TA(X)	1201	1204	$A_1(F_2)$
19		2LA(L)	1182	1187	$A_1(F_2)$
20	9	TO(X)+TA(X)	1170	1168	$A_1(F_2)$
21		$2A_1$(W)	1152	1148	$A_1(F_2)$
22		LO(L)+TA(L)	1108	1104	A_1, F_2
23	10	TO(L)+TA(L)	1038	1044	$A_1(F_2)$
24		TA(X)+LA(X)	1012	1015	A_1, F_2
25		TA(L)+LA(L)	842	845	A_1, F_2

a) Refs. [48,49].

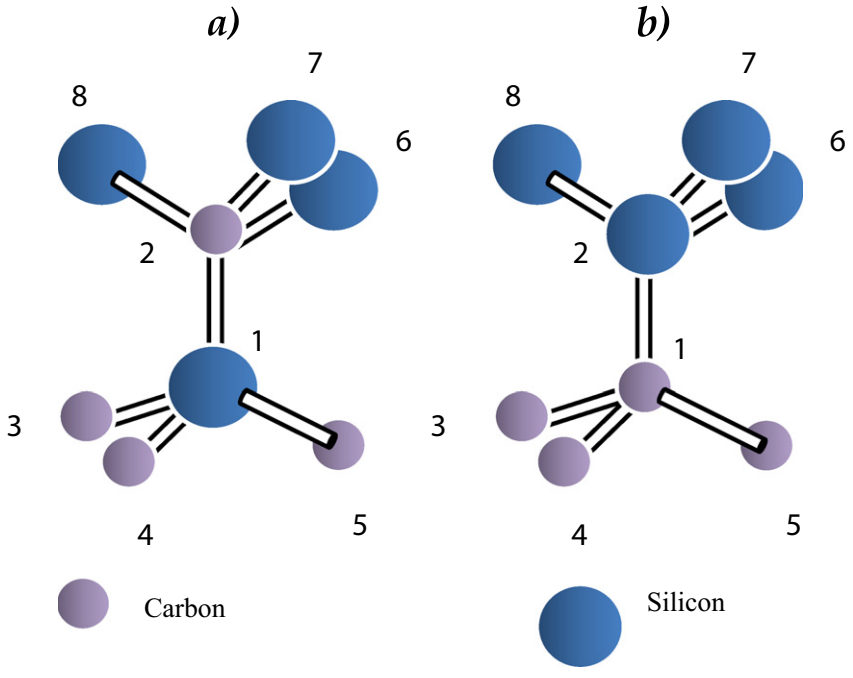

Fig. 4. Perturbation models for (a) an isolated defect (T_d symmetry) occupying Si- or C-site and (b) NN anti-site pair Si_C–C_{Si} defect (C_{3v}) symmetry in the *zb* 3C–SiC.

gap modes in different irreducible representations by solving the real part of the determinant:

$$\prod_{\mu\Gamma} \det|I - G_o^{\mu\Gamma}(\omega)P^{\mu\Gamma}(\omega)| = 0. \quad (10)$$

Here, $G_o^{\mu\Gamma}$ is the Green's function of the perfect crystal projected on to the defect space and $P^{\mu\Gamma}(\omega)$ is the perturbation matrix in a given irreducible representation.

2.7. Perturbation matrices

In any defect calculation, the most important issue is to give an adequate representation to the impurity perturbation. For studying the dynamical behavior of defects by expending GF theory, we have constructed perturbation matrices {***P***} by appropriately including the mass change at the defect sites and the effects of lattice relaxations to account for the 'impurity-host' interactions. For substitutional defects, the lattice relaxations in the vicinity of Si/C are estimated by using Harrison's semi-empirical BOM [31,32]. In terms of the Hartree–Fock atomic term values, the method provides simple analytical expressions [32] for the change in impurity–host ΔE_b and host–host $\Delta E'_b$ bond energies and suggests a computationally efficient and logical way to estimate the bond-length distortions Δd by setting $\left[\frac{\partial}{\partial \Delta d}\left(\Delta E_b + \Delta E_b^{'}\right) = 0\right]$. In Fig. 5, we have displayed the BOM calculation of $\Delta d/d$ as a function of change in bond energies for 3C–SiC:Si — revealing a ~16.3% out-ward bond-length distortion. The estimated values of $\Delta d/d$ caused by several isolated defects including anti-sites Si_C (+0.163), C_{Si} (−0.134) reported in Table 3 are compared favorably well with the first-principles calculations [21–23]. These results have clearly played the vital roles for appraising changes in the force constants caused by isolated defects in 3C–SiC. In the framework of a RIM and exploiting the scaling behaviors of $\Delta d/d$ with the NN force constant variations t and u, we have constructed perturbation {***P***} matrices for various isolated and pair defects following the method described in Ref. [33].

2.8. Impurity modes of isolated defects

In 3C–SiC, the calculated impurity-vibrational modes are examined as a function of t and u, for several isolated defects occupying Si and C-sites (T_d symmetry) by solving Eq. (10) in different irreducible A_1, E and F_2 representations. One must note that while the DFT calculations have insinuated both A_1 and F_2 gap modes for isolated anti-site Si_C defect in 3C–SiC [20] — our GF simulations established, however, only the F_2 local- and gap-modes for lighter impurities occupying Si-sites (see: Fig. 6a–b)) and the F_2 gap-modes for heavier impurities on C sites (see: Fig. 6c)), respectively. By including the appropriate force constant variations for the isolated B_{Si}, {C_{Si}; (Si_C)} defects in 3C–SiC, our calculations of impurity vibrations have projected triply degenerate F_2 local-mode to appear near ~1044 cm^{-1} and gap-mode near ~635 cm^{-1} {local mode ~1038 cm^{-1} and gap mode ~630 cm^{-1} mode; (gap mode ~660 cm^{-1})}. By retaining the values of 'impurity–host' bonding for anti-site defects, we have also evaluated the real (full lines) and imaginary (dashed lines) parts (see: Fig. 7a–b)) of det $\left|\overleftrightarrow{I} - \overleftrightarrow{G}^{o}_{F2}(\omega)\overleftrightarrow{P}_{F2}(\omega)\right|$ for *a*) C_{Si} and *b*) Si_C defects in 3C–SiC. To the best of our knowledge, there exists no experimental data of the LVMs for B_{Si} — our GF calculations of the gap modes for isolated anti-site C_{Si}, Si_C defects in 3C–SiC compare moderately well with the RS experiments and other DFT [20–25] simulations.

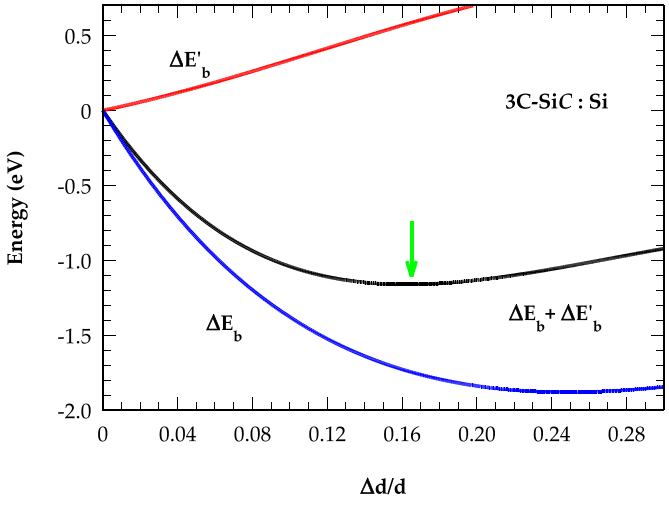

Fig. 5. Change in impurity-host ΔE_b, host–host $\Delta E'_b$ and total energy per bond ($\Delta E_b + \Delta E'_b$) as a function of distortion $\Delta d/d$ in 3C–SiC:Si system. The green arrow indicates the calculated distortion.

Table 3
Calculated impurity-host bond length $d + \Delta d$ in (Å) and distortions $\Delta d/d$ caused by various isolated defects occupying C and Si sites in 3C–SiC with d — being the perfect bond length (1.887 Å). Negative and positive signs of $\Delta d/d$ correspond to the inward and out-ward distortions of the nearest neighbors, respectively.

	Bond-length variation for isolated defects in 3C–SiC		
	Defect	$\Delta d/d$[a]	$(d + \Delta d)$[a]
3C–SiC			
	Si_C	0.163; 0.24[b];0.16[c]	2.194
	N_C	−0.056	1.781
	O_C	−0.108	1.683
	P_C	0.098	2.071
	B_C	0.059	2.000
3C–SiC			
	C_{Si}	−0.134; −0.10[b]; −0.12[c]	1.634
	Al_{Si}	0.037	1.957
	B_{Si}	−0.088	1.721
	Ge_{Si}	0.143	1.914
	P_{Si}	−0.042	1.808

[a] This work.
[b] Ref. [21].
[c] Ref. [22.]

2.9. Impurity modes of NN pair-defects

The role of intentionally doped shallow/deep defects (e.g., B, Al, N, P etc.) in 3C–SiC has been extensively studied [21–23]. The substitutional incorporation of such dopants in one or the other sub-lattice sites can be promoted by tuning Si/C ratio either during the growth activity or in the co-implantation process. While the formation of "complex-centers" involving intrinsic and doped defects are speculated — the identification of such defect-centers have not been firmly established. Again, in 3C–SiC there exists a limited knowledge about the realization of different intrinsic–defect complexes in as-grown and ion-implanted/electron-irradiated procedures as well as their assuring reactions over the heat treatments. As mentioned before (cf. Section 1) our first-order RS measurement has identified two weak impurity modes near ~625 and 670 cm^{-1} in V-CVD grown 3C–SiC samples [28]. The former mode (at ~625 cm^{-1}) occurring close to the edge of the acoustic phonon band continuum is assigned as a triply degenerate F_2 gap mode of C_{Si}. The later unresolved Raman band (at ~670 cm^{-1}) with a relatively large (~8 cm^{-1}) full width at half maximum is designated as the F_2 gap mode of Si_C (cf. Section 2.8). The temperature dependent profile of the ~670 cm^{-1} band has indicated disordering caused by adjacent defects and/or stress that made the phonon life time shorter to instigate mode broadening.

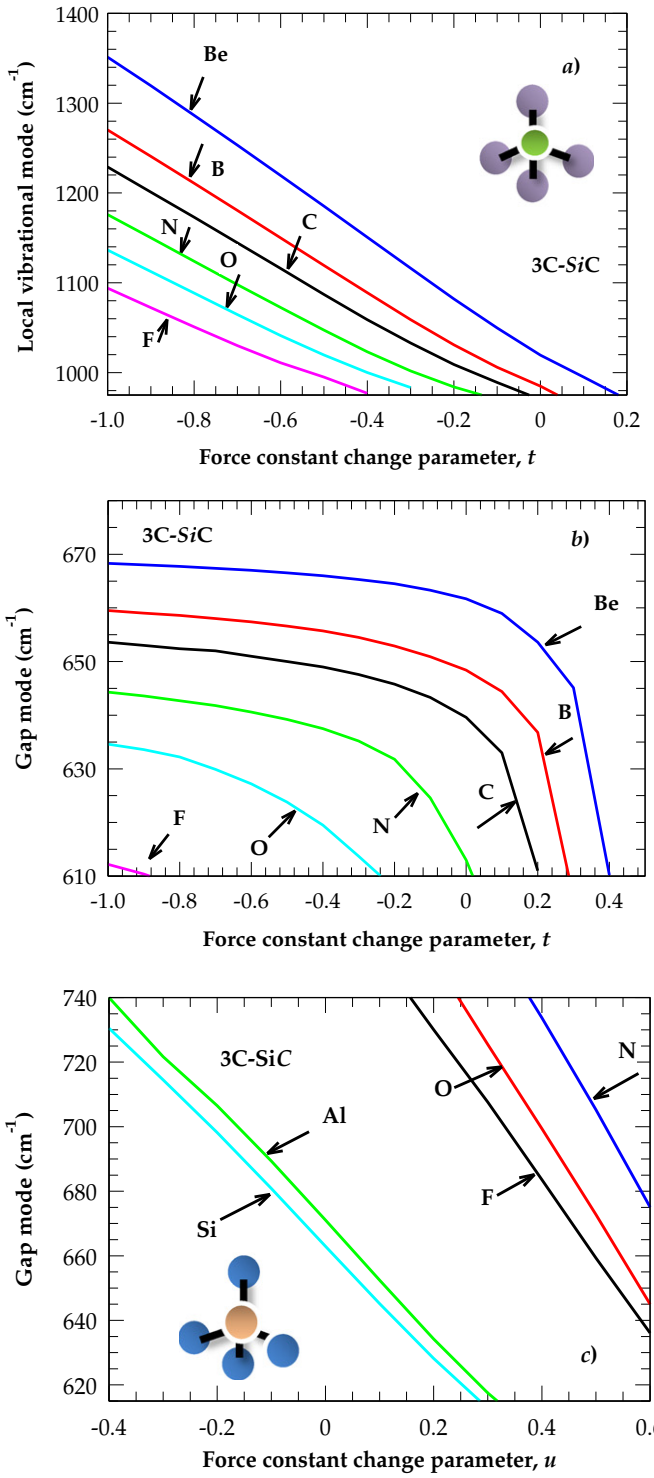

Fig. 6. (a) Calculated frequencies of the F_2 localized vibrational modes, (b) gap modes for defects occupying Si-site versus the force constant change parameter t and (c) gap modes for defects occupying C-site versus the force constant change parameter u in 3C–SiC.

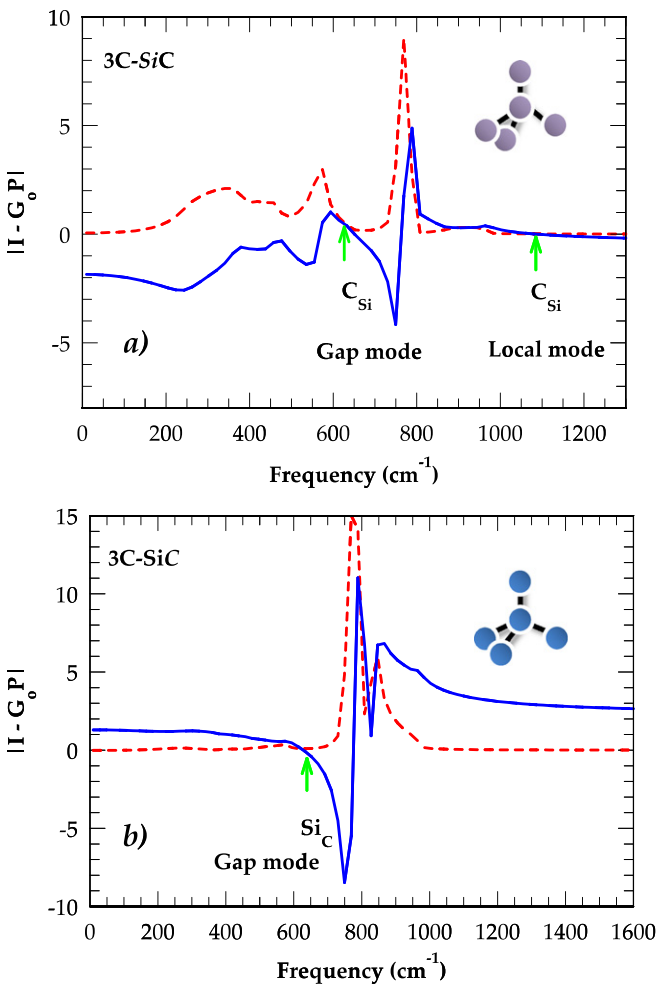

Fig. 7. (a) Calculated real (solid line) and imaginary (dotted line) parts of det $|\boldsymbol{I} - \boldsymbol{G_oP}|$ in the F_2 representation showing gap and local modes of (a) C_{Si} in 3C–SiC, and gap mode (b) Si_C in 3C–SiC.

In Section 2.8, we have reported our GF results for the impurity vibrations of various isolated defects (T_d-symmetry), including C_{Si} and Si_C. One must note that a triply-degenerate F_2 gap-mode of an isolated Si_C defect can split-up into a nondegenerate a_1 and doubly degenerate e modes, if it forms a pair with another impurity atom occupying the NN Si-site (I_{Si}). Next, we described our GF simulations of LVMs in 3C–SiC for the NN pair defects (C_{3v}-symmetry). For assessing the impurity vibrations of a neutral ASP ('Si_C–C_{Si}'), we have maintained (see: Fig. 4b)) the estimated values of u and t for isolated anti-site (Si_C, C_{Si}) defects and included both mass change ε_1 and force constant variation F_{12} ($\equiv u + t - ut + \Gamma_{12}$) between the pair defect by setting $\Gamma_{12} = 0$ (cf. Section 2.6). As expected, our GF calculation for the neutral ASP defect has offered a splitting of the triply degenerate F_2 gap-mode of an isolated Si_C into a non-degenerate a_1 mode near ~664.8 cm^{-1} (or 83.1 meV) and a doubly-degenerate e mode at ~660.6 cm^{-1} (or 82.6 meV). The other two impurity modes are perceived, however, to merge into the 3C–SiC phonon-continuum regime. Again, one must note that the two simulated gap mode frequencies of the ASP defect lies well within the FWHM (~8 cm^{-1}) of the broad band observed near ~670 cm^{-1} (or 83.8 meV) in RS experiments [28]. By exploiting the high resolution IR and RS spectroscopy, we are in the process of studying both local and gap modes in the co-implanted 3C–SiC material samples to identify the NN (B_{Si}–N_C) and/or NNN (B_C–N_C; Al_{Si}–P_{Si}) donor–acceptor-pairs (DAPs) [51]. The simulations reported here by GF theory can certainly be helpful in evaluating the impurity mode fingerprints to classify the DAP structures.

3. Discussion

For isolated antisite C_{Si} and Si_C defects in 3C–SiC, our GF simulations have predicted F_2 gap modes near ~630 cm^{-1} and ~660 cm^{-1}, respectively in good agreement with RS [28] and other optical data [20]. Unlike DFT study of LVMs for Si_C, where both A_1 (~644 cm^{-1}) and F_2 (~671 cm^{-1}) modes are suggested in the gap region [20] — our

calculations recognized, however, only the F_2 gap-mode to emerge near ~660 cm^{-1}. By including appropriate force constant variations in the NN neutral ASP defect of C_{3v}-symmetry the GF simulations provided values of two gap-modes appearing well within the FWHM of the unresolved broad RS (~670 cm^{-1}) band at ~664.8 cm^{-1} (83.1 meV) (a_1) and ~660.6 cm^{-1} (82.6 meV) (e), respectively. These results extended strong corroboration to recent reports [1–3] that both isolated antisite (Si_C, C_{Si}) and ASP are favorable defects in SiC and the phonon-assisted RS spectroscopy is sensitive in providing fingerprints for extracting information about the nature and microscopic structure of complex defect centers [26].

It is equally intriguing to note that our calculated gap modes of neutral ASP in 3C–SiC has insinuated a possible link to the prototypical D_I center, for which the LT PL measurements have revealed two phonon lines at ~668.7 cm^{-1} (83.4 meV) and ~661.3 cm^{-1} (82.7 meV) [20] to be allied to the a_1- and e- modes. Again, the intensity difference between the observed modes can be justified by Group-theoretic selection rules apposite to C_{3v}-point-group symmetry [52]. While the D_I spectra in SiC polytypes consisted of sharp zero–phonon lines (ZPLs) L_i accompanied by broad phonon-assisted structure — the traits of ZPLs are ascribed to bound-exciton recombination at the iso-electronic defect centers [20–25]. Accordingly, models of different atomic structures are proposed for the D_I center with distinct PL lines observed in SiC polytypes after performing diverse irradiation procedures, as well as in as-grown materials and epilayers having different levels of n- or p-type residual doping. None of the recommended models, however, seem to be adequately assuring and conclusive [20–25]. In 3C–SiC, a study based on LT PL experiments and ab initio supercell calculations suggested a neutral ASP defect to be a good candidate for the D_I center — where the simulated one-electron level close to the measured ZPL line (L_1 ~ 1.97 eV) of Si_C–C_{Si}, the LVMs, and the hyperfine constants in its paramagnetic state have all justified the viability of the model. However, reports by other groups using local DFT and molecular dynamics simulations [22–25] inferred a low thermal stability for the NN Si_C–C_{Si} — thus discarding the ASP model, as D_I center is found stable at higher (up to 2000 K) temperatures. While alternative schemes are alluded linking Si_C [23] and Si_C–$(C_{Si})_2$ complex [22] to the D_I defect — both of these models have been rejected [25] as well. Again, Hornos et al. [19] have advocated for carbon–silicon interstitial aggregates to play important roles in the formation of D_I center. However, we oppose this assignment based on our GF calculations of LVMs for Si_i–C_i in 3C–SiC that yielded gap mode values far from experiments and predicted high frequency modes that have not been even perceived [51]. From the calculated formation energies we do agree, however, that self-interstitials may help create Si_C, C_{Si} and Si_C–C_{Si} in both irradiated SiC as well as in CVD grown epifilms at high Si/C ratio [17]. Again, it is interesting to note that the DFT results of LVMs (~660 and 669 cm^{-1}) for the Si_C–$(C_{Si})_2$ are found comparable with the GF values of gap-modes (660.6 and 664.8 cm^{-1}) for a neutral ASP. Our GF study has led us to believe that for the D_I center, an ASP model fits the measurements [20,28] because the calculated gap modes not only explained the broad RS feature but also the doublet observed in the LT PL spectrum.

4. Summary and conclusion

In summary, we have reported comprehensive experimental and theoretical studies to probe the structural, optical, phonon, thermal and defect properties of V-CVD grown 3C–SiC/Si (001) samples. Accurate assessments of lattice dynamical, SORS, thermal and defect properties are made by incorporating phonons from a RIM [29] fitted to the IXS [30] data. In the first-order RS besides observing the conventional long wavelength optical modes [TO(Γ) ~796 cm^{-1}, LO(Γ) ~973 cm^{-1}] in free standing 3C–SiC films, we have recognized [28] two additional weak phonon features near ~625 and 670 cm^{-1} — possibly falling between the forbidden gap of acoustic and optical branches. Temperature dependent profile of the unresolved Raman mode near ~670 cm^{-1} indicated [28] potential disordering caused by nearby defects and/or stress that could have rendered shorter phonon lifetime to instigate mode broadening. In conclusion, our GF study has led us to believe that for the D_I center, an ASP model fits the experiments well, as the gap modes not only justified the broad RS feature but also the doublet seen in the LT PL spectrum.

Acknowledgments

The author wishes to thank the Dean, College of Natural Science and Mathematics for the travel support and for Innovation Grant that he received from the School of Graduate Studies at Indiana University of Pennsylvania, Indiana, PA that made this collaborative research possible. The experimental results on Raman scattering, photoluminescence and EXAFS spectroscopy were provided by Professor Zhe Chuan Feng (National Taiwan University, Taipei) on V-CVD grown 3C–SiC/Si(001) samples prepared by Professor Chin-Che Tin (University of Malaya, Malaysia).

References

[1] F. La Via, M. Camarda, A. La Magna, Mechanisms of growth and defect properties of epitaxial SiC, Appl. Phys. Rev. 1 (2014) 031301.
[2] S. Rajasekhara, B.H. Neuner III, C.A. Zorman, N. Jegenyes, G. Ferro, G. Shvets, P.J. Ferreira, D. Kovar, The influence of impurities and planar defects on the infrared properties of silicon carbide films, Appl. Phys. Lett. 98 (2011) 191904.
[3] N. Yang, H. Zhuang, R. Hoffmann, W. Smirov, J. Hess, X. Jiang, C.E. Nebel, Nanocrystalline 3C–SiC electrode for biosensing applications, Anal. Chem. 83 (2011) 5827.
[4] Matteo Bosi, Bernard E. Watts, Giovanni Attolini, Claudio Ferrari, Cesare Frigeri, Giancarlo Salviati, Antonella Poggi, Fulvio Mancarella, Alberto Roncaglia, Oscar Martińez, Vanesa Hortelano, Growth and characterization of 3C–SiC films for micro electro mechanical systems (MEMS) applications, Cryst. Growth Des. 9 (4852) (2009).
[5] J.D. Reddy, A.A. Volinsky, C.L. Frewin, C. Locke, S.E. Saddow, Mechanical properties of 3C–SiC films for MEMS applications, Mater. Res. Soc. Symp. Proc. 1049 (2008) AA03–AA06.
[6] D.J. Young, J. Du, C.A. Zorman, W.H. Ko, Applications of SiC-based thin films in electronic and MEMS devices, IEEE Sensors 4 (2004) 464.
[7] B.J. Baliga, Silicon Carbide — Power Devices, World Scientific, Singapore, 2005.
[8] Silcon carbide: recent major advances, in: W.J. Choyke, H. Matsunami, G. Pensl (Eds.), Springer-Verlag, Berlin2004;
Advances in Silicon carbide-Processing and Applications, in: Stephen E. Saddow, Anant Agarwal (Eds.), Artech House, Inc., Boston2004.
[9] Z.C. Feng (Ed.), SiC Power Materials — Devices and Applications, Springer, Berlin2004.
[10] Silicon Carbide: Materials, Processings and Devices, in: Z.C. Feng, J.H. Zhao (Eds.), vol. 20, Taylor & Francis Books Inc., New York2003.
[11] Philip G. Neudeck, VLSI Technology, in: Wai-Kai Chen (Ed.), CRC Press2003 (Chap. 6).
[12] Chen Da, Z. YuMing, Z. YiMin, W. YueHu, J. RenXu, Characterization of the heteroepit axial growth of 3C–SiC on Siduring low pressure chemical vapor deposition, Chin. Sci. Bull. 55 (2010) 3102.
[13] A.M. Hashim, K. Yasui, Low temperature heteroepitaxial growth of 3C–SiC on silicon substrates by triode plasma chemical vapor deposition using dimethylsilane, J. Appl. Sci. 8 (2008) 3523.
[14] C.S. Roper, V. Radmilovic, R.T. Howe, R. Maboudian, Characterization of polycrystalline 3C–SiC films deposited from the precursors 1,3-disilabutane and dichlorosilane, J. Appl. Phys. 103 (2008) 084907.
[15] A. Gupta, D. Paramanik, S. Varma, C. Jacob, CVD growth and characterization of 3C–SiC thin films, Bull. Mater. Sci. 27 (2004) 445.
[16] Haiwu Zheng, Junjie Zhu, Fu. Zhuxi, Bixia Lin, Xiaoguang Li, Heteroepitaxial growth and characterization of 3C–SiC films on Si substrates using LPVCVD, J. Mater. Sci. Technol. 21 (536) (2005).
[17] C.C. Tin, R. Hu, R.L. Coston, J. Park, Reduction of etch pits in heteroepitaxial growth of 3C–SiC on silicon, J. Cryst. Growth 148 (1995) 116.
[18] W.J. Choyke, L. Patrick, Photoluminescence of radiation defects in cubic SiC: localized modes and Jahn–Teller effect, Phys. Rev. B 4 (1971) 1843.
[19] T. Hornos, N.T. Son, E. Janźen, A. Gali, Theoretical study of small silicon clusters in 4H–SiC, Phys. Rev. B 76 (2007) 165209.
[20] A. Gali, P. Deák, E. Rauls, N.T. Son, I.G. Ivanov, F.H.C. Carlsson, E. Janzán, W.J. Choyke, Correlation between the antisite pair and the D_I center in SiC, Phys. Rev. B 67 (2003) 155203;
A. Gali, P. Deák, E. Rauls, N.T. Son, I.G. Ivanov, F.H.C. Carlsson, E. Janzán, W.J. Choyke, Optically detected magnetic resonance studies of intrinsic defects in 6H–SiC, Semicond. Sci. Technol. 14 (1999) 1141.
[21] M. Posselt, F. Gao, W.J. Weber, Atomistic simulations on the thermal stability of the antisite pair in 3C– and 4H–SiC, Phys. Rev. B 73 (2006) 125206.
[22] M.V.B. Pinheiro, E. Rauls, U. Gerstmann, S. Gerlich-Weber, H. Overhof, J.-M. Spaeth, Silicon vacancy annealing and D_I luminescence in 6H–SiC, Phys. Rev. B 70 (2004) 245204.
[23] T.A.G. Eberlein, R. Jones, S. Öberg, P.R. Briddon, Density functional theory calculation of the D_I optical center in SiC, Phys. Rev. B 74 (2006) 144106;

T.A.G. Eberlein, R. Jones, S. Öberg, P.R. Briddon, Alphabet luminescence lines in 4H–SiC, Phys. Rev. B 65 (2002) 184108.
[24] U. Gerstmann, A.P. Seitsonen, D. Ceresoli, F. Mauri, H.J. von Bardeleben, J.L. Cantin, J. Garcia Lopez, Si_CC_{Si} antisite pairs in SiC identified as paramagnetic defects with strongly anisotropic orbital quenching, Phys. Rev. B 81 (2010) 195208.
[25] Jérémie Lefèvre, Jean-Marc Costantini, Didier Gourier, Stéphane Esnouf, Guillaume Petite, Characterization of a silicon-related defect detected by its excited triplet state in electron-irradiated 3C–SiC, Phys. Rev. B 83 (075201) (2011).
[26] Hiroshi Harima, Properties of GaN and related compounds studied by means of Raman scattering, J. Phys. Condens. Matter 14 (R967) (2002).
[27] Devki N. Talwar, Zhe Chuan Feng, Jyh-Fu Lee, P. Becla, Extended x-ray absorption fine structure and micro-Raman spectra of Bridgman grown $Cd_{1-x}Zn_xTe$ ternary alloys, Mat. Res. Exp. 1 (2014) 015018.
[28] Devki N. Talwar and Zhe Chuan Feng, Chin-Che Tin and Chee Wee Liu (unpublished).
[29] K. Kunc, Dynamique de Réseau de Composés AN B8 — N Présentant la Structure de la. *Blende*, Ann. Phys. (Paris) 8 (319) (1973) 74.
[30] J. Serrano, J. Strempfer, M. Cardona, M. Schwoerer-Böhning, H. Requardt, M. Lorenzen, B. Stojetz, P. Pavone, W.J. Choyke, Determination of the phonon dispersion of zinc blende (3C) silicon carbide by inelastic x-ray scattering, Appl. Phys. Lett. 80 (2002) 4360.
[31] W.A. Harrison, Electronic Structure and the Properties of Solids, Freeman, San Francisco, 1980.
[32] D.N. Talwar, K.S. Suh, C.S. Ting, Lattice distortion associated with isolated defects in semiconductors, Philos. Mag. B56 (1987) 593.
[33] Devki N. Talwar, Zhe Chuan Feng, Tzuen-Rong Yang, Vibrational signatures of isotopic impurities and complexes in II–VI compound semiconductors, Phys. Rev. B 85 (2012) 195203.
[34] D.W. Feldman, J.H. Parker, W.J. Choyke, L. Patrick, Phonon dispersion curves by Raman Scattering in SiC, polytypes 3C, 4H, 6H, 15R, and 21R, Phys. Rev. 173 (1968) 787;
Raman Scattering in ***6H*** SiC, 1701968. 698.
[35] C.-Z. Wang, R. Yu, H. Krakauer, Pressure dependence of born effective charges, dielectric constant, and lattice dynamics in SiC, Phys. Rev. B 53 (5430) (1996).
[36] K. Karch, P. Pavone, W. Windl, O. Schütt, D. Strauch, Ab initio calculation of structural and lattice-dynamical properties of silicon carbide, Phys. Rev. B 50 (1994) 17 054.
[37] Priya Vashishta, Rajiv K. Kalia, Aiichiro Nakano, José Pedro Rino, Interaction potential for silicon carbide: a molecular dynamics study of elastic constants and vibrational density of states for crystalline and amorphous silicon carbide, J. Appl. Phys. 101 (2007) 103515.
[38] B.Y. Thakore, S.G. Khamboja, A.Y. Vahora, N.K. Bhatt, A.R. Jani, Thermodynamic properties of 3C–SiC, Chin. Phys. B 22 (2013) 106401.
[39] V.L. Gurvich, I.V. Veyts, Thermodynamic Properties of Individual Substances, Hemisphere Publishing Corp., New York1972.
[40] Goldberg Yu, M.E. Levinshtein, S.L. Rumyantsev, in: M.E. Levinshtein, S.L. Rumyantsev, M.S. Shur (Eds.), Properties of advanced semiconductormaterials GaN, AlN, SiC, BN, SiC, SiGe, John Wiley & Sons, Inc., New York, 2001, pp. 93–148;
G.A. Slack, S.F. Bartram, Thermal expansion of some diamond like crystals, J. Appl. Phys. 46 (1975) 89.
[41] E.L. Kern, D.W. Hamill, H.W. Deem, H.D. Sheets, Thermal properties of β-silicon carbide from 20 to 2000 °C, Mater. Res. Bull. 4 (1969) 25.
[42] M.V. Klein, Theory of two-phonon Raman scattering in transition metals and compounds, Phys. Rev. B 24 (1981) 4208.
[43] C. Trallero-Giner, A. Cantarero, M. Cardona, One-phonon resonant Raman scattering: Fröhlich exciton-phonon interaction, Phys. Rev. B 40 (1989) 4030.
[44] C.H. Grein, S. Zollner, M. Cardona, Microscopic theory of second-order Raman scattering in silicon under uniaxial stress, Phys. Rev. B 43 (1991) 6633.
[45] W. Windl, K. Karch, P. Pavone, O. Schütt, D. Strauch, W.H. Weber, K.C. Hass, L. Rimai, Second-order Raman spectra of SiC: experimental and theoretical results from ab initio phonon calculations, Phys. Rev. B 49 (1994) 8764;
W. Windl, K. Karch, P. Pavone, O. Schütt, D. Strauch, Full ab initio calculation of second-order Raman spectra of semiconductors, Int. J. Quantum Chem. 56 (1995) 787.
[46] P.-L. Dulong, A.-T. Petit, Recherches sur quelques points importants de la Théorie de la Chaleur, Ann. Chim. Phys. (in French) 10 (1918) 395–413.
[47] A.M. Karo, J.R. Hardy, Precise vibrational frequency distributions and the second-order Raman spectrum and specific heat of NaCl, Phys. Rev. 141 (1966) 696;
Room-Temperature Second-Order Raman Spectra of CsCl, CsBr, and CsI, Phys. Rev. 160 (1967) 702;
Lattice Dynamics and Second-Order Raman Spectrum of NaF, Phys. Rev. 179 (1969) 837.
[48] J.L. Birman, Space group selection rules: diamond and zinc blende, Phys. Rev. 127 (1962) 1093;
Theory of Infrared and Raman Processes in Crystals: Selection Rules in Diamond and Zincblende, Phys. Rev. 131 (1963) 1489.
[49] W.G. Nielson, Raman spectrum of cubic ZnS, Phys. Rev. 182 (1969) 838.
[50] S. Rohmfeld, M. Hundhansen, L. Ley, Raman scattering in polycrystalline 3C–SiC: influence of stacking faults, Phys. Rev. B 58 (1998) 9858.
[51] Devki N. Talwar and Zhe Chuan Feng (unpublished).
[52] G.W. Ludwig, H.H. Woodbury, in: F. Seitz, D. Turnbull, H. Ehreneich (Eds.), Solid State Physics, 2nd ed., vol. 13, Academic, New York, 1962, p. 223.